



The ESRF dark-field x-ray microscope at ID06

Kutsal, M.; Bernard, P.; Berruyer, G.; Cook, P. K.; Hino, R.; Jakobsen, A. C.; Ludwig, W.; Ormstrup, Jeppe; Roth, T.; Simons, Hugh

Total number of authors:
17

Published in:
I O P Conference Series: Materials Science and Engineering

Link to article, DOI:
[10.1088/1757-899X/580/1/012007](https://doi.org/10.1088/1757-899X/580/1/012007)

Publication date:
2019

Document Version
Peer reviewed version

[Link back to DTU Orbit](#)

Citation (APA):
Kutsal, M., Bernard, P., Berruyer, G., Cook, P. K., Hino, R., Jakobsen, A. C., Ludwig, W., Ormstrup, J., Roth, T., Simons, H., Smets, K., Sierra, J. X., Wade, J., Wattecamps, P., Yildirim, C., Poulsen, H. F., & Detlefs, C. (2019). The ESRF dark-field x-ray microscope at ID06. *I O P Conference Series: Materials Science and Engineering*, 580(1), Article 012007. <https://doi.org/10.1088/1757-899X/580/1/012007>

General rights

Copyright and moral rights for the publications made accessible in the public portal are retained by the authors and/or other copyright owners and it is a condition of accessing publications that users recognise and abide by the legal requirements associated with these rights.

- Users may download and print one copy of any publication from the public portal for the purpose of private study or research.
- You may not further distribute the material or use it for any profit-making activity or commercial gain
- You may freely distribute the URL identifying the publication in the public portal

If you believe that this document breaches copyright please contact us providing details, and we will remove access to the work immediately and investigate your claim.

The ESRF dark-field x-ray microscope at ID06

M Kutsal^{1,2}, P Bernard¹, G Berruyer¹, P K Cook¹, R Hino¹, A C. Jakobsen¹, W Ludwig^{1,3}, J Ormstrup², T Roth¹, H Simons², K Smets⁴, J X Sierra⁵, J Wade^{1,2}, P Wattecamps¹, C Yildirim^{1,6}, H F Poulsen² and C Detlefs¹

¹ European Synchrotron Radiation Facility, 38043 Grenoble, France

² Department of Physics, Technical University of Denmark, 2800 Kgs. Lyngby, Denmark

³ MATEIS, INSA-Lyon, 69621 Villeurbanne Cedex, France

⁴ LAB Motion Systems, 3001 Leuven, Belgium

⁵ Department of Energy, Technical University of Denmark, 4000 Roskilde, Denmark

⁶ OCAS, Pres. J.F. Kennedylaan 3, BE-9060, Zelzate, Belgium

E-mail: detlefs@esrf.fr

Abstract. We present an instrument for dark-field x-ray microscopy installed on beamline ID06 of the ESRF — the first of its kind. Dark-field x-ray microscopy uses full field illumination of the sample and provides three-dimensional (3D) mapping of micro-structure and lattice strain in crystalline matter. It is analogous to dark-field electron microscopy in that an objective lens magnifies diffracting features of the sample. The use of high-energy synchrotron x-rays, however, means that these features can be large and deeply embedded. 3D movies can be acquired with a time resolution of seconds to minutes. The field of view and spatial resolution can be adapted by simple reconfiguration of the x-ray objective lens, reaching spatial and angular resolution of 30-100 nm and 0.001°, respectively. The instrument furthermore allows pre-characterization of samples at larger length scales using 3DXRD or DCT, such that a region of interest (e.g. a single grain) can be selected for high-resolution studies without the need to dismount the sample. As examples of applications we show work on mapping the subgrains in plastically deformed iron and aluminum alloys, mapping domains and strain fields in ferroelectric crystals, and studies of biominerals. This ability to directly characterize complex, multi-scale phenomena *in-situ* is a key step towards formulating and validating multi-scale models that account for the entire heterogeneity of materials. As an outlook, we discuss future prospects for such multi-scale characterization by combining DFXM with 3DXRD/DCT, and coherent x-ray methods for coarser and finer length-scales, respectively.

1. Introduction

Many, if not most, technological materials are composed of crystalline elements that are hierarchically organized over length scales ranging from millimeters to nanometers, spanning up to 6 orders of magnitude. The same is true for biominerals, ice, sand and geological materials in general. Crystalline elements and substructures such as grains, domains and atomic-scale defect networks determine many of the macroscopic physical and mechanical properties of these materials. Understanding the interplay of physical phenomena and structural dynamics at, and between, these different lengths scales is therefore a critical and persistent issue across materials and geological sciences. Our understanding, however, is still limited by the lack of a non-destructive three-dimensional (3D) probe of the local crystal lattice (structure, strain,

and orientation) that can be rapidly switched between different length scales and that enables acquisition of movies during processing.

The need to probe the local crystallography favours a diffraction-based approach. Existing 3D techniques, however, have shortcomings with respect to multi-scale characterization. Electron-based methods can provide very high spatial resolution, but are either limited to thin foils [1, 2] or involve serial sectioning [3, 4]. Scanning [5, 6, 7, 8, 9, 10] and coherent [11, 12, 13, 14, 15, 16, 17, 18] x-ray methods are rapidly progressing towards 20 nm resolution, but are limited to small sampling volumes. Furthermore, all methods face the challenge that the illuminated part of a bulk sample may comprise millions or even billions of structural elements whose diffracted signals overlap, rendering data analysis and interpretation complicated and in many cases impossible.

Aiming to overcome these limitations, dark-field x-ray microscopy (DFXM) is a full-field imaging technique for non-destructive mapping of the structure, orientation, and strain of deeply embedded crystalline elements in 3D [19, 20, 21, 22, 23, 24]. By placing an x-ray objective lens in the diffracted beam, direct space resolutions of 30–100 nm can be reached while maintaining a comfortable working distance of 10 cm or more between the sample and x-ray lens. The spatial resolution and field of view can be adapted by changing the focal length of the lens and thus “zooming” in or out. Furthermore, through its narrow angular and real space field of view, the objective also filters stray diffraction signals, suppressing unwanted overlap and isolating the individual structural element of interest.

As a first implementation of the method a dedicated dark-field x-ray microscope was recently installed on beamline ID06 of the European Synchrotron Radiation Facility (ESRF, Grenoble, France). The instrument is designed to combine DFXM with coarse scale 3D grain mapping techniques such as 3D X-Ray Diffraction (3DXRD) [25, 26, 27, 28, 29] and diffraction contrast tomography (DCT) [30, 31], as well as classical tomography and diffraction topography. This combination enables the user to rapidly progress from fast overviews of the entire specimen to detailed studies of local phenomena in a single experimental setting, without the need to dismount the sample.

Following an introduction to DFXM, in this article we present the **instrumentation** of the microscope at ID06, providing details on all relevant hardware components. In particular we present the refractive optics used for condensing and imaging. Compound refractive lenses (CRLs) were until recently the only choice, providing a reasonably large field of view but being limited in terms of spatial resolution by lens aberrations. As a newly developed alternative, multilayer Laue lenses (MLLs) offer larger numerical apertures (NAs) and improved spatial resolution, at the expense of a smaller field of view and reduced working distance. Next, we demonstrate the performance of the instrument on three selected examples in materials science: the processing of plastically deformed metals, the distribution of strain and orientation gradients in ferroelectrics, and hierarchical organization in bio-minerals.

1.1. The geometry and principle of DFXM

The geometry and operational principle of dark-field x-ray microscopy (see figure 1) is conceptually similar to dark-field transmission electron microscopy (TEM): the diffracted beam passes through an x-ray objective lens, creating a magnified image of a specific region of interest with contrast from local variations in lattice symmetry, orientation and strain [21]. The sample-to-detector distance $d_1 + NT + d_2$ is 2–6 m, enabling magnification ratios of up to 50 while still maintaining sufficient space around the sample for complex sample environments.

A defining feature of the dark-field x-ray microscope is the x-ray objective. Like a visible light microscope, the x-ray objective can be reconfigured to adjust the magnification, field-of-view, and numerical aperture, hence allowing adjustment of the spatial resolution according to specific experimental requirements. So far primarily compound refractive x-ray lenses made of

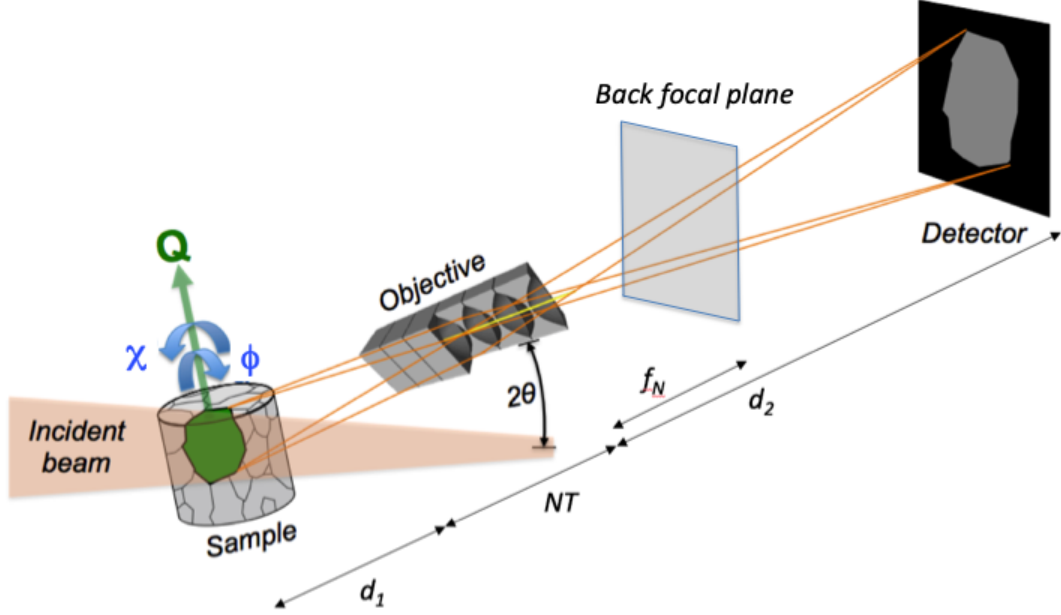


Figure 1. Principle of dark-field x-ray microscopy. Monochromatic x-rays illuminate a crystalline element of interest, and the diffracted radiation is imaged by means of an x-ray objective and a 2D detector. The objective is here a compound refractive lens, comprising N lenslets each with a thickness of T . d_1, d_2, f_N are the sample plane-entry of CRL distance, exit of CRL – image plane distance and the focal distance, respectively. Scanning the sample tilt (χ, ϕ), and scattering (2θ) angles facilitate mapping of orientation and axial strain respectively, while different projections can be obtained by rotating the sample about its scattering vector, \vec{Q} .

Beryllium [32] or SU-8 polymer [33] have been used. Their performance is discussed below along with a presentation of the first results using multilayer Laue lenses as objectives — with the aim to improve the spatial resolution. Irrespective of the choice, the imaging system is associated with a Fourier plane, the back focal plane downstream of the objective, see figure 1. Similar to dark field microscopy operation in a TEM, the direct space (imaging) information in the image plane and the Fourier space (diffraction) information in the back focal plane may be combined in a variety of ways [22].

Like the TEM, the dark-field x-ray microscope can be operated in a variety of modes. Most experiments so far have used a one-dimensionally-focusing condenser to create a narrow line-beam [34] that illuminates a ‘layer of the material (typically $200 \mu\text{m} \times 200 \mu\text{m} \times 200 \text{nm}$), which is then imaged at an oblique angle. Experiments typically involve the use of a succession of modalities including

- *Rocking curve imaging in section topography:* The dependence of the intensity on the Bragg angle (rocking scan) is analyzed pixel by pixel. It is possible to combine rocking curve imaging in magnified and non-magnified (using a near-field camera, see below) modes

without unmounting the sample.

- *Mosaicity scans*: By systematically varying the sample tilts, χ and ϕ , a spatially resolved local pole figure can be acquired [21].
- *Strain scans*: By scanning longitudinally (θ - 2θ -scan) the strain component along the scattering vector is imaged [21]. Typically, this is combined with a rocking scan or with integration over the rocking profile at each 2θ setting. As an alternative, strain mapping may be performed in the back focal plane [22].
- *Reciprocal space maps*: A high resolution reciprocal space map of the illuminated volume is available either in the back focal plane [22] or in the far-field regime (see below).

3D mapping can be performed in two ways. Firstly, by stacking layers of the kind described above. This is performed by translating the sample through the planar beam in small increments. A second, faster method is *magnified topo-tomography*. Here, projections of the sample are acquired while the sample is rotated about the scattering vector [35, 21], and a 3D representation is reconstructed using tomographic principles. Again, data can be taken in magnified and non-magnified mode. Experimental protocols and reconstruction codes for magnified topo-tomography are currently under development.

By setting 2θ to zero, magnified bright field imaging is obtainable [36, 37]. Translating the sample along the optical axis makes it possible to acquire pure absorption contrast images or phase contrast images at any Fresnel number. Moreover, by placing a phase plate in the back focal plane, Zernike type phase contrast images are created [38].

When based on the use of CRLs, the entire imaging system is accurately described by geometrical optics. However, the length of the CRL, NT , tends to be of the same order as the focal length f_N , implying that the thin lens approximation is not valid. Analytical expressions for the NA, field of view, depth of field, and spatial resolution in bright field mode are provided in [39]. For dark field microscopy, operating in the image plane, expressions for the resolution in both direct space and reciprocal space spatial resolution are provided in [21]. Correspondingly, in [22] equations are provided for the reciprocal space resolution in the back focal plane and the corresponding strain resolution.

1.2. Complementary imaging on longer length scales

It is necessary to combine DFXM with more traditional imaging in order to identify local regions of interest and to provide overviews during processing studies. The microscope at ID06 enables this in several ways:

- A *near-field camera* with high resolution placed close to the sample can provide classical absorption or phase contrast tomography, non-magnified diffraction topographies, and DCT measurements.
- A *diffraction camera* with large pixels can provide 3DXRD type mapping as well as classical (sample averaged) diffraction information.
- *Far-field imaging* can provide high resolution reciprocal space maps [27]. Conveniently this modality can be obtained with the same detector as shown in figure 1 by simply translating the objective out of the diffracted beam.

More details about these cameras are provided below.

2. Description of beamline components

2.1. Overall beamline layout and optical scheme

The beamline is located at the high-beta straight section ID06 of the ESRF in Grenoble, France. It consists of one white beam optics hutch, OH, and two monochromatic beam experimental

Table 1. Undulator parameters obtained from fits of the observed gap with maximum flux as function of photon energy to the theoretical curve.

		U18 CPMU	U27
Min. gap	[mm]	6.05	11
Max. gap	[mm]	30	300
Period λ_u	[mm]	18.25(2)	27.19(2)
B_0	[T]	2.44(2)	1.93(2)
α		1.10(1)	1.00(1)

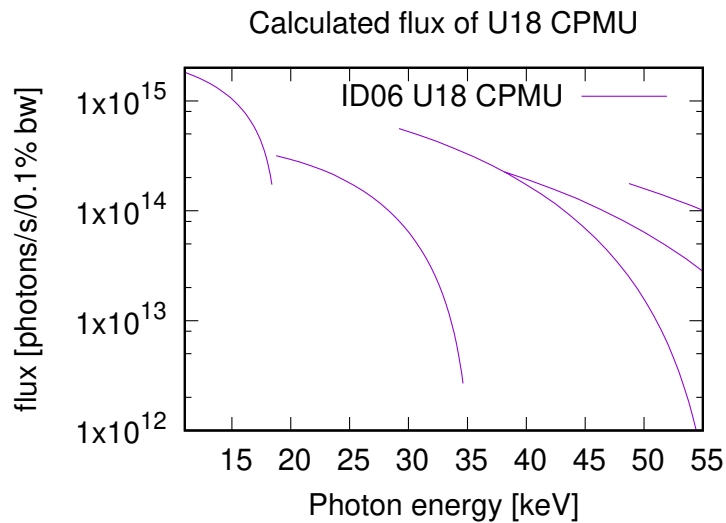


Figure 2. Calculated flux of the ID06 U18 CPMU undulator as function of photon energy, in photons per second into a $1 \times 2 \text{ mm}^2$ aperture at 28 m from the source, and for a 0.1% band width. This calculation is for the pre-upgrade ESRF, without taking into account absorption in diamond and Beryllium windows.

hutches, EH1 and EH2. OH houses standard ESRF high power primary slits, a UHV section where temporary white beam experiments can be set up [40, 41, 37], the monochromator, secondary slits and intensity monitor, a Transfocator, and, finally, the safety shutter for EH1. The dark-field x-ray microscope is implemented in EH1, whereas EH2 houses the Large Volume Press (LVP) that is described elsewhere [42].

The coordinate system used at ID06 has x along the beam axis, y horizontal and away from the storage ring, and z upwards.

2.2. Source

Two source devices are installed in the straight section (see Table 1): A U18 cryogenic permanent magnet in-vacuum undulator (CPMU) with minimum gap 6 mm [43] covers the energy ranges from 11–20 keV and 33–100 keV, see figure 2. Additionally a U27 out-of-vacuum permanent magnet undulator with minimum gap 11 mm covers the energy ranges 7.5–11 keV below the fundamental, and 20–33 keV in between the fundamental and third harmonic of the U18.

2.3. Monochromator

The ID06 double crystal monochromator, located in OH at 35.8 m downstream of the nominal source point, is the first optical element of the beamline apart from a 300 μm diamond window that separates the beamline and storage ring vacuum systems, and the white beam primary slits located 27.8 m downstream of the source. The monochromator was designed and built by Cinel Strumenti Scientifici (Vigona, Italy) to ESRF specifications. It has been in continuous operation on ID06 since 2008. It houses two pairs of flat crystals in Bragg-Bragg geometry mounted side by side. By horizontally translating the entire monochromator vessel, either symmetric Si(111) or Si(311) reflections can be selected. The Bragg angle θ can be adjusted between 2.05° to 53.5° , covering 2.46–55 keV using the Si(111) pair of crystals, and 4.72–105 keV using the Si(311) pair. In practice, the vast majority of experiments uses the Si(111) pair. The monochromator is operated in fixed exit geometry with an offset of $z = +15$ mm between the white and monochromatic beams.

The peak monochromatic flux at the sample position is $\approx 10^{13}$ photons/s at 11 keV, with an unfocused spot size of $\approx 1 \text{ mm}(h) \times 0.5 \text{ mm}(v)$.

2.4. Transfocator

The UHV Transfocator [44] is located in OH at a distance of 38.7 m from the source point. The mechanical design is based on in-vacuum piezo-actuators for groups of lens elements. The vacuum chamber can be moved in y , z , pitch and yaw to align the optical axis of the Transfocator to the beam (ESRF in-house design, which is based on a similar device at Petra III [45]). It contains sets of 1D (vertically focusing) and 2D (bi-dimensionally focusing) compound refractive lenses made of Be (RXOptics, Juelich, Germany) that can be moved into and out of the beam in groups. The Transfocator can be used as a collimator or pre-focusing device. Due to the ratio of the distances towards the source and the sample, however, the demagnification of 1:3.9–1:4.8 (depending on the position of the main block of the instrument) remains fairly moderate. For larger demagnification, i.e. smaller spot size or line height at the sample position, condenser optics can be employed close to the sample, see section 2.5.3. The installed lenses allow collimation from 7.5–30 keV and focusing from 7.5–30 keV.

2.5. Microscopy bench

The hard x-ray microscope was implemented in the existing experiments hutch EH1 of ID06. The design was therefore restricted by the existing infrastructure and beamline optics as described above.

A Be exit window at 52.4 m from the source ends the UHV section of the beam path. The remainder of EH1 is utilized by the microscopy bench and far-field detector frame, see figure 3. The beam travels in air, without flight paths.

The design goal of the hard x-ray microscope was to achieve a resolution better than 50 nm. For this, optimum mechanical stability is required on short (vibrations) and long (thermal drifts) time scales. Due to its high density, high damping factor and low thermal expansion coefficient, granite is very well suited as the construction material.

In particular, the relative position of the sample and objective lens is critical, as any differential movement of these elements will be amplified in the far-field detector by the geometrical magnification. Common-mode vibrations, however, are not magnified. We have therefore chosen to implement the critical elements on a common granite support (the “main block”), which can be moved on air pads on a support bench, also made from granite. In choosing the position of the main block a compromise has to be made between the maximum scattering angle (limited by the maximum height of the far-field detector, favoring position further downstream) and maximum geometrical magnification (limited by the focal length of the objective lens and the distance to the far-field detector, favoring a position further upstream).

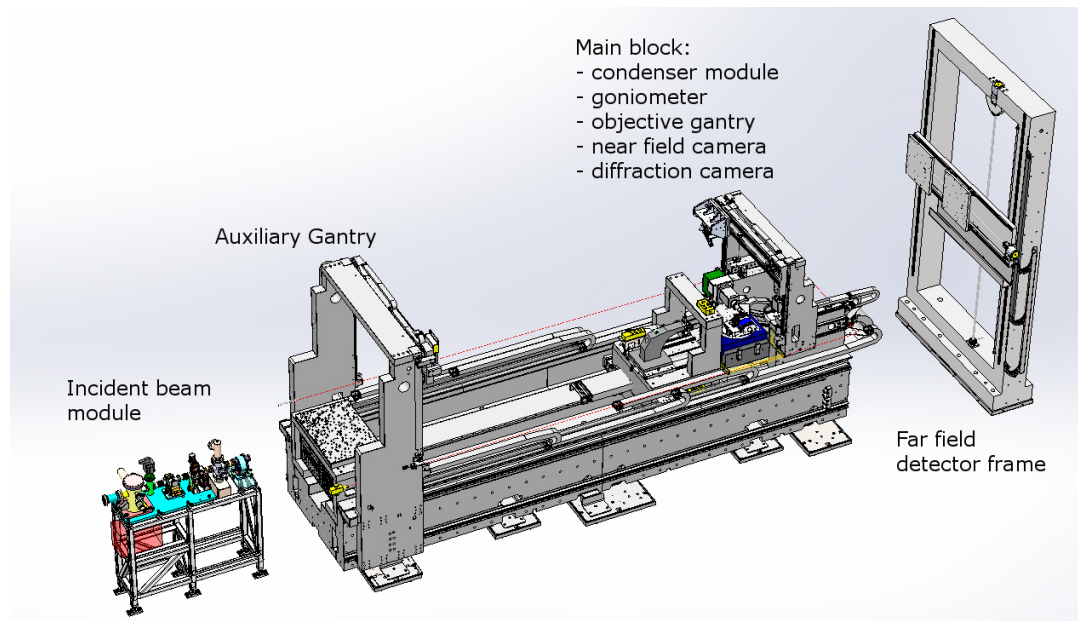


Figure 3. The microscopy bench. Along the beam (left to right), elements are: Incident beam module, main block with condenser module, goniometer, near-field camera, objective gantry and diffraction camera. The auxiliary gantry can be moved along the entire length of the bench. The far-field detector frame is located at the downstream end of the hutch.

The support bench, main block, and alignment mechanics were designed and built by LAB motion systems (Leuven, Belgium) to ESRF specifications. An overview is shown in figure 3, further details on the different components are given below.

The bench is assembled from several granite blocks, whose weight was limited by the capacity of the available overhead crane (6 t). Its total weight is about 22 t. It is mounted on 13 adjustable Wedgmount levelers (AirLoc Schrepfer, Oetwil am See, Switzerland) – this lucky number is the result of the blocks being individually supported to aid with their relative alignment before they are rigidly bolted together. Steel plates have been set in the concrete floor to spread the load, provide a flat and level mounting surface, and to anchor the tension bars of the levelers. The complete bench can be disassembled, e.g. to remount it on a different beamline. It is, however, also possible to inject epoxy resin under the bench to permanently bond it to the concrete floor. The bench is 6 m long and 1.4 m wide. The air bearing surface is 0.5 m above the floor.

2.5.1. Incident beam module The incident beam module consists of a 0.6 m long optical bread board mounted in fixed position at the upstream end of the bench, 53.7 m from the source. The optical elements on it are (upstream to downstream):

- Beam position monitor based on a quadrupole ionization chamber and ESRF Quadera error amplifier. The vertical beam position detected here is used for feedback on the monochromator’s second crystal pitch.
- Secondary slits (AT-F7-AIR, JJ X-ray, Hoersholm, Denmark) at 53.9 m from the source.
- Decoherer (optional) a spinning disk of graphite (Goodfellow 613 136 00) to produce a fluctuating wave front that will average out any speckle from structure in the incident beam’s wave front [46].

- Ionization chamber intensity monitor (ESRF design). The ionization chamber can be moved out of the beam by a motorized translation to insert a beam profile monitor (ESRF design using a Basler ace acA1300-30gm CCD camera and Infinity InfiniStix 2× objective) or visible light mirror reflecting a pre-aligned laser beam as an alignment aid.
- Fast shutter, synchronized with the exposure signal of the different cameras.

2.5.2. Main block The main block serves as common support for the sample goniometer and for optical elements in close vicinity of the sample, i.e. condenser, near-field camera, diffraction camera, and objective. It can be moved on air pads along the length of the bench. For experiments, its position is typically fixed and the air is turned off. The main block is 2.3 m long and can be translated by 2.8 m.

2.5.3. Condenser The condenser unit is the first element on the main block. A translation stage with 340 mm stroke along x can be equipped with a small hexapod (H-824, Physik Instrumente, Karlsruhe, Germany) and compact Transfocator (ESRF in-house development) with Be lenses for moderate focusing, or a granite arch with y , z , pitch and yaw alignment mechanics for Si, polymer or multilayer Laue lenses for more aggressive focusing. Downstream of the lenses a set of 4-blade motorized slits (AT-F7-AIR, JJ X-ray, Hoersholm, Denmark) and a compact ionization chamber (ESRF design) for intensity monitoring can be mounted.

In recent practice, the most frequently used condenser is a set of 58 vertically focusing 1D Be lenses with apex radius of curvature $100\ \mu\text{m}$ (RXOptics, Juelich, Germany) mounted in a fixed enclosure on the hexapod. This is used in conjunction with 2D lenses in the OH Transfocator to optimize the flux on the entrance pupil of the condenser. A set of 1D SU-8 polymer lenses (KIT, Karlsruhe, Germany) for use at higher photon energies is under commission.

2.5.4. Sample goniometer The sample goniometer is mounted on the main block, downstream of the condenser. By moving the main block, the sample can be positioned between 53.6 and 56.4 m from the source and, correspondingly, between 2.2 and 5.0 m from the plane of the far-field detector frame (see section 2.6).

The sample goniometer is assembled from several components. The goniometer base consists of two orthogonal air-bearing rotation stages rotating about the z (outside) and y (inside) axes, and an air-bearing y -stage. It was designed and manufactured by LAB motion systems (Leuven, Belgium) to INSA (Lyon, France) and ESRF specifications. The goniometer provides high quality rotational movement about the horizontal and vertical axes of each respective air bearing rotation stage – the large rotation stage about the z axis has a maximum rotational error of 36 nm and axial error of 23 nm, and the smaller rotation stage about the y axis has a maximum rotation error of 80 nm and axial error of 56 nm. The center of rotation can be aligned to the beam axis by the goniometers y -stage and a stepper motor driven z -stage (AXMO, Brétigny/Orge, France) underneath the goniometer.

Shown in figure 4 is the part of the goniometer that is closest to the sample. Mounted on the horizontal ω rotation stage are a motorized crossed swivel stage (SA04B-RS, Kohzu, Japan) for the “sample tilts” ϕ and χ , and a piezo-based xyz micropositioner for sample centering (SmarAct, Oldenburg, Germany).

The goniometer pre-dates the dark field microscopy project. Its configuration allows for rotations about a horizontal scattering vector (“topo-tomo” or azimuthal scan) [30, 31] when the Bragg angle is set by the outside z rotation stage. As, due to the asymmetry of the source, the preferred scattering geometry is in the vertical plane, the goniometer should be replaced by a new instrument optimized for topo-tomo in the vertical scattering plane, i.e. with a y -rotation stage outside and z -rotation stage inside [21].

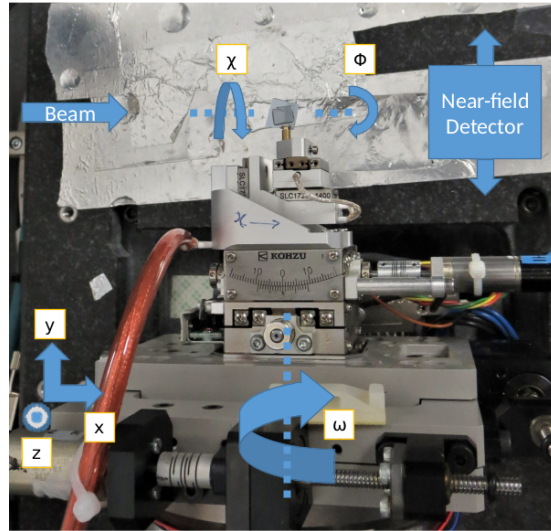


Figure 4. View of goniometer: LAB goniometer, Kohzu tilts and SmarAct xyz stage. Showing beam direction in blue, xyz coordinate system, and goniometer axes of rotation.

2.5.5. Near-field camera The near-field camera is an indirect detector, consisting of a thin scintillator, x-ray transparent mirror, and an optical microscope coupled to a CCD camera. The optics were designed and built by Optique Peter (Lentilly, France) to ESRF specifications. The semi-transparent scintillator can be positioned within millimeters of the sample, e.g. for classical tomography or for DCT-type experiments [30, 31]. Free-standing gadolinium gallium garnet (GGG) single crystals of $25\ \mu\text{m}$ and $50\ \mu\text{m}$ thickness are available, as well as thinner scintillator films on a substrate. The objective lens (Mitutoyo M-Plan Apo 10x/0.28 or 5x/0.14) is protected from radiation damage by a lead glass window. Optical parameters of the near-field camera are listed in table 2. The CCD camera is a ESRF FreLoN 2K camera [47].

In addition to xyz linear alignment axes, the near-field camera is mounted on a rotation table to swing it out of the way when other optical elements, such as the objective lens, need to be positioned in close proximity to the sample, or when a full 360° rotation about the goniometers z axis is required for alignment purposes.

Table 2. Optical parameters of the different cameras of the dark field microscope.

CCD	pixel size	Magnification			Effective	Field of
	$[\mu\text{m}^2]$				pixel size	view
		Objective	Tube lens	Eye piece	$[\mu\text{m}^2]$	$[\text{mm}^2]$
Near-field camera						
Atmel TH7899M	14×14	5x 10x	0.9x	2.5x	1.24×1.24 0.62×0.62	2.49×2.49 1.24×1.24
Diffraction camera		Fiber taper				
Atmel TH7899M	14×14	(0.296x)			47.3×47.3	94.6×94.6
Wide-field far field camera		Objective (12 mm f/1.8)				
Sony ICX445	3.75×3.75	≈0.08x			48×48	62×45
High resolution far field camera		Objective	Tube lens			
Atmel TH7899M	14×14	10x	0.9x		1.56×1.56	3.1×3.1

2.5.6. Diffraction camera The diffraction camera is a fiber-taper coupled FreLoN camera [48, 47] with effective pixel size (after distortion correction) of $47.3\ \mu\text{m} \times 47.3\ \mu\text{m}$, and field of view $94.6\ \text{mm} \times 94.6\ \text{mm}$ (see table 2). The camera can be inserted at a distance of 180 to 560 mm downstream of the sample, or be removed completely from the beam path to make room for the objective lens or auxiliary optics and detectors.

It is equipped with a movable beam stop which in turn can be equipped with a photodiode to monitor the intensity of the direct beam. The purpose of the diffraction camera is to record complete diffraction rings at elevated photon energies in order to reconstruct 3D grain maps of the sample using 3DXRD techniques [25, 26, 27, 28]. Grains thus determined can then be studied with ultimate resolution using dark field microscopy or, eventually, coherent techniques.

2.5.7. Objective The objective stage allows for xyz , pitch and yaw adjustment of an objective lens. The pitch (model 5202.60) and yaw (model 410) stages were supplied by Huber Diffraktionstechnik (Rimsting, Germany). The linear and angular travel ranges are large enough to keep the lens aligned with the axis of a diffracted beam up to scattering angles (2θ) of 30° .

The centers of rotation of the pitch and yaw stages intersect in the center of the lens assembly. For rotations about the sample position, e.g. for varying the scattering angle 2θ during strain scans, the rotations therefore have to be combined with the appropriate translations. The objective stages center of rotation can be positioned between 0 and 380 mm downstream of the sample. The finite length of the lens assemblies imposes further practical limits. In the y - z plane the objective stage can be moved up to 500 mm away from the beam axis.

Mechanically, the objective stage is implemented as a gantry with two lead screw drives for the x - and z - motions, and one lead screw drive for the y -motion. The x and z motions need to be driven simultaneously to avoid skew motions and eventual mechanical damage to the system. This is handled through the ESRF Icepap’s “linked axis” firmware option. The x , y and z -stages are equipped with pneumatic clamps to further improve the mechanical stability when at fixed position.

During the conception of the objective gantry particular attention was paid to minimizing thermal and vibration effects, as the relation of these movements relative to the sample are significantly magnified on the far-field camera based upon the ratios shown in figure 1. Thermal

Table 3. Parameters of the different objective lenses. E is the working energy, NA the numerical aperture, N and T the number and distance between lens elements, and f is the focal length.

	E [keV]	NA [mrad]	Resolution [nm]	$N \times T$ [mm]	f [mm]
Be	17	0.55	≈ 100	$68 \times 1.6 + 20 \times 2.0$	277
SU-8	33	0.18	≈ 140	$(65(h) + 65(v)) \times 0.77$	330
MLL	17.3	2(h), 1.6(v)	≈ 30	–	9.5(h), 13.7(v)
MLL	34.5	0.4(h), 0.7(v)	≈ 30	–	37(h), 40(v)

stability was ensured by the choice of granite as the base material linked with the stabilization of the climate in EH1, and reducing wherever possible the thickness of materials with higher coefficients of expansion. To create a rigid structure to reduce the vibration effects, this led to several developments in the placement of rails and sliding carriages to ensure the maximum possible rigidity based on space and translation constraints. This can be seen particularly in the gantry legs whereby two rails have been mounted each side at 90 degrees to each other, which provides a better average stiffness in the z and y axes. The rails are also spaced apart and the lower rail provides a strong lever arm against the vibrations in the tops of the structure.

After measuring the frequency response of the objective gantry was found to have its first harmonic at 40 Hz. Given the size of the gantry, this is encouraging and correlates with the original computer simulations completed by both the ESRF and LAB Motion Systems.

At present, three different types of objective lens are used for microscopy experiments:

Beryllium CRL Low absorption and high ratio of refractive index decrement over absorption (δ/β) make Beryllium in theory the best CRL material at all photon energies [49]. For working energies of ≈ 15 – 20 keV we therefore use a CRL of 88 2D Be lenses with apex radius of curvature of $50 \mu\text{m}$ (RXOptics, Juelich, Germany). In practice the CRLs are limited by aberration to a resolution around 100 nm.

Optical parameters of the Be CRL are summarized in table 3.

SU-8 polymer CRL The chromaticity of the CRL (focal length is approximately proportional to the square of the working energy) limits the practical use of Be in objective lenses to working energies below ≈ 20 keV.

While Si-based lenses can potentially achieve very high resolution [50, 51, 39], strong absorption limits their apertures to very small values, which in turn dictates very short working distances – thus the resolution obtained under the practical working conditions of a materials science x-ray microscope (working distance ≈ 100 – 300 mm) is much worse than the ultimate limit of ≈ 50 nm that has been demonstrated in optics tests.

SU-8 polymer lenses as developed by the IMT group at KIT present an interesting solution for working energies above 20 keV, combining manufacturing precision, homogeneous material and cost-effectiveness [33].

Optical parameters of the SU-8 CRL are summarized in table 3.

Multilayer Laue lenses Recently we successfully tested Multilayer Laue Lenses (MLLs) as objectives for both phase and diffraction contrast imaging [52]. MLLs can have a NA 10 times better than compound refractive lenses, and virtually no manufacturing errors [53]. MLLs are therefore a candidate for achieving a spatial resolution as good as 10 nm or alternatively 10–100

times faster data acquisition. Similar to Si refractive lenses, however, the MLLs available today have small physical apertures and thus require very short working distances [54].

Optical parameters of the two MLL objective lenses that have been tested on the instrument are summarized in table 3. Further optimization in terms of both manufacturing (a larger physical aperture) and alignment is required, but the work is seen as encouraging.

2.5.8. Auxiliary gantry The auxiliary gantry is a xyz alignment stage that can travel along the entire length of the bench. It allows the mounting of additional optical elements for future experiments beyond simple microscopy. Possible uses include the insertion of slits, phase shifters or cameras upstream of the condenser or between the objective lens and far-field detector, e.g. in the back focal plane.

2.6. Far-field detectors

The far-field detector frame is located at the downstream end of EH1, separate from the support bench. It allows yz positioning of two detectors, a wide-field detector and a high resolution detector. It consists of a granite frame with y and z translation stages (AXMO, Brétigny/Orge, France), a cradle that can be inclined to orient the cameras perpendicular to the diffracted beam (Design et Mécanique, Montaud, France), and the detectors.

The far-field detector frame is located 60.64 m downstream of the source, i.e. between 2.2 and 5.0 m downstream of the sample, depending on the position of the main block. Its travel range (using the high resolution detector and direct beam axis as reference points) is -0.8 to $+0.6$ m in the horizontal (y) and -0.5 to $+2.3$ m in the vertical (z) direction.

2.6.1. Wide-field far camera This is a simple indirect detector based on a plastic scintillator screen, Linos MeVis-C 12mm f/1.8 machine vision lens, and a C-mount CCD camera (Basler acA1300-30gm). Details are given in table 2.

2.6.2. High resolution detector The high resolution detector is an indirect detector composed of a scintillator screen (typically $10\ \mu\text{m}$ LuAG:Eu on a $170\ \mu\text{m}$ YAG substrate) [55], optical microscope with Olympus UIS2 UPlanSApo 10x/0.40 objective and Olympus U-TLU-1-2 tube lens. The optical microscope is operated without an eye piece, projecting the intermediate image directly onto an ESRF FreLoN camera [47] with 2048×2048 pixels. This combination yields an effective pixel size of $1.56 \times 1.56\ \mu\text{m}^2$ and a field of view of $3.1 \times 3.1\ \text{mm}^2$. The thickness of the scintillator screen is a compromise between quantum efficiency (x-ray absorption) and resolution (due to the limited depth of field of the objective) [56].

The narrow field of view of the high-resolution camera can make finding the diffracted beam somewhat challenging. To facilitate this, both cameras are rigidly mounted on the same support. It is thus possible to first locate and center the diffracted beam in the wide-field camera, and to then switch to the high resolution camera by simply translating the camera support by the predetermined spacing between the cameras.

For dark field microscopy in the horizontal scattering plane (e.g. topo-tomo experiments with the present goniometer), an additional far-field detector can be mounted on a table equipped with y and z translations and a rotation about the z axis. The detector configuration is identical to the high-resolution far-field detector described above.

3. Examples

Below we provide three examples of DFXM applications. Other lines of work performed so far include imaging of dislocations within semiconductors and oxides [23], and processing studies of fuel cells [57].

3.1. Deformed metals and alloys

When a pure metal or a metallic alloy is plastically deformed, dislocations self organize into walls surrounding defect-free regions known as cells or subgrains with a size of $\approx 1 \mu\text{m}$. Moreover, these cells organize into intricate patterns inside existing grains. During subsequent annealing the stored energy is released by the processes of recovery and recrystallisation. In the former the cells refine and strain is released. In the latter new strain-free grains are nucleated and grow at the expense of the deformed matrix. Recovery and recrystallisation co-exist within the sample. Electron microscopy has been extensively used for post mortem studies of both the plastic deformation and the annealing phenomena. DFXM provides a unique opportunity to study these multi-scale phenomena *in situ* from deeply embedded grains within $\approx \text{mm}$ -sized specimens [19, 58, 59, 24].

In a first example, DFXM was used to study a deeply embedded alpha iron grain within a $330 \mu\text{m}$ thick sample of Fe with 850 ppm Nitrogen [24]. Prior to the experiment, the sample was solutionized at 580 C for 15 hours. Using a 33 keV full field beam and the SU-8 polymer lens as objective, projections were acquired. The exposure time was 1 s. The high angular resolution of DFXM enables us to resolve the mosaic spread in the rocking (θ) and rolling (χ) directions, within the grain. Despite the annealing the mosaicity map of the (110) reflection shows a substantial angular spread (figure 5(a)). The orientation gradient in this figure can be resolved with EBSD. The local misorientation, however, falls below the angular resolution of conventional EBSD.

In a second example, DFXM was used to study a deeply embedded recrystallized grain in a 50% recrystallized Al 1050 alloy [19]. A cross-sectional layer was illuminated with a condensed line beam and imaged with the Be CRL as objective at 17 keV with exposure time of 1 s. The mosaicity map presented in figure 5(b) clearly shows the subgrain structures separated by low-angle boundaries within the recrystallized grain.

In a recent experiment, we have generalised DFXM to allow observation of the microstructure in highly deformed materials of key industrial interest. Specifically the microstructural changes during *in-situ* annealing of a steel sample deformed to a true strain of $\epsilon \approx 2$ were studied (to be presented elsewhere [60]).

3.2. Strain and domain mapping in ferroelectrics

Ferroelectric, ferroelastic and multiferroic materials are typified by the presence of domains: distinct regions of similar lattice orientation, separated by atomically-coherent domain walls (e.g. inversion about a zone axis) [61]. In response to stresses, electric fields, or other perturbations, these domain structures self-organize via the collective motion of domain walls. Given the strong anisotropy of many of these materials, the modulation of domain structures is often accompanied by significant macroscopic responses (e.g. changes in the dielectric and piezoelectric coefficients). These large responses are widely utilized in a range of applications including shape-memory alloys, digital memory and solid-state capacitors. Furthermore, the discovery of emergent phenomena at the domain walls (e.g. photoelectricity) has renewed interest in the local structure at and around such walls [62]. The ability to quantitatively probe the lattice strain and misorientation in the vicinity of the domain walls is expected to yield important insights into what drives these emergent phenomena.

Here, DFXM was used to reveal the domain structure embedded within a bulk single crystal of barium titanate (BaTiO_3). Figure 6 shows the image intensity acquired in a single exposure, which shows clear contrast from the individual domains. Given the 001-orientation of the crystal, it is evident that the domain walls lie on $\langle 110 \rangle$ lattice planes, and that the domain walls are not completely straight. The curvature of domain walls in this manner indicates the presence of underlying electric or elastic heterogeneities, such as vacancies or dislocations, that cause the walls to distort from their lowest-energy configuration. The key advantage of investigating such

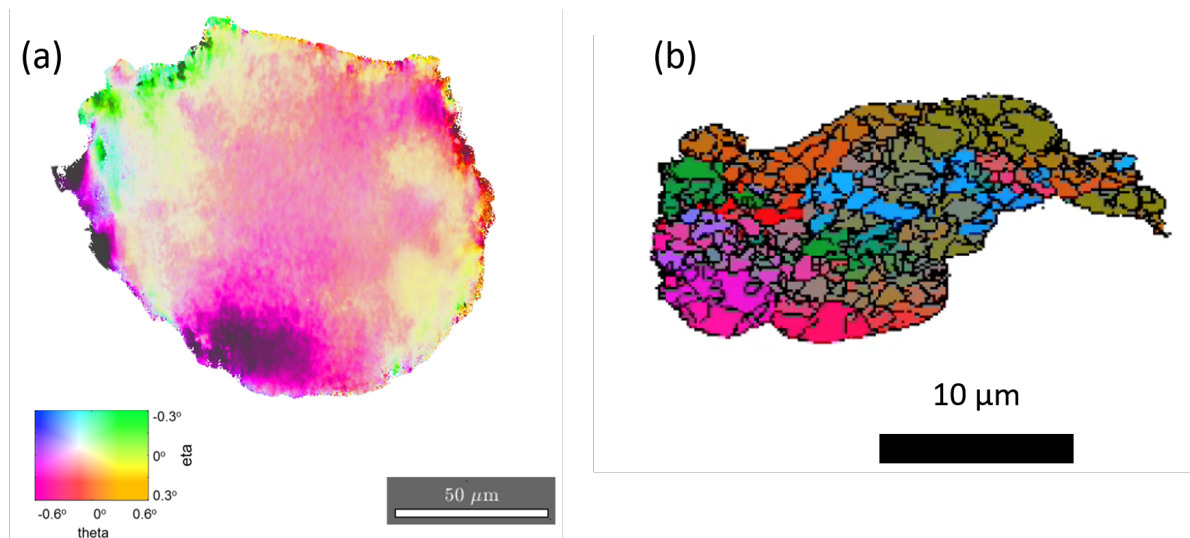


Figure 5. (a) Mosaicity map of a Fe-850 ppmN grain after annealing at 580 C for 15 h. This is a projection image with the color code indicating angular variation within parts of a (110) pole figure. (b) Mosaicity map of a layer within a recrystallized grain in 50% recrystallized Al 1050. The colors indicates angular variation within parts of a (200) pole figure.

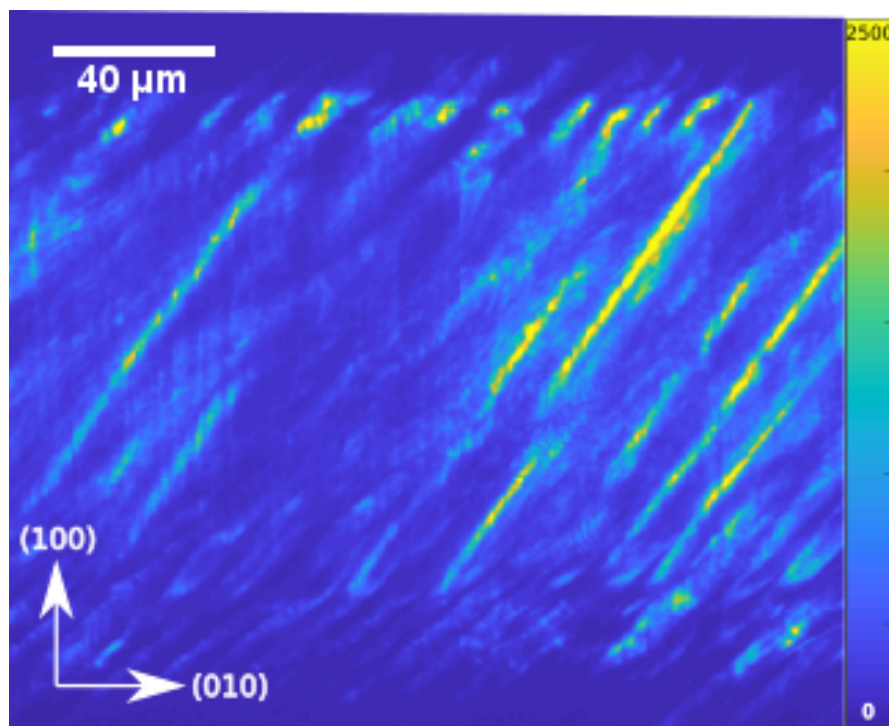


Figure 6. Dark field x-ray microscopy image of domains embedded in a single crystal of BaTiO_3 . The domain walls are clearly curved, indicating the presence of underlying elastic or electric heterogeneities. The color code to the right indicates intensity in arbitrary units.

domain structures using DFXM is that it is a full-field imaging technique. As such, full images of embedded domain structures may be captured in a single exposure within a second or less. This allows for dynamic studies of multiscale structures under applied electric fields or at elevated temperatures [63]. These measurements are key to understanding and accurate modelling of ferroelectricity and ferroelasticity, and are directly comparable to multi-scale models, such as phase-field and Monte-Carlo simulations.

Shown in figure 7 are the first DFXM results using the MLL as the objective. The figure shows a map of the average lattice misorientation from a projection through the BaTiO₃ crystal. The ferroelastic domain walls are clearly visible as diagonal lines aligned with the 110 direction of the sample. In this map, the transition region between neighbouring domain orientations at the domain wall is in the order of 1 μm thick. The map also shows a clear misorientation between the top and bottom parts of the image, which is likely to be attributable to an out-of-plane domain wall along 101-type planes. This allows the local lattice distortions at the intersection of the 101- and 110-oriented domain walls to be investigated directly and in detail.

3.3. Microstructure of biominerals

Biominerals are hierarchical materials found throughout nature [64]. Examples are widespread, including bone, tooth, corals, shells, and otoliths. Biominerals form as a combination of inorganic mineral and organic template under strict biological control by the organism, yielding an exceptional control of final structure in both crystallography and habit [64]. This control has evolved to yield materials whose properties are optimized for particular functions, such as wear resistance for teeth, or strength and crack resistance for protective shells [64]. Like nature, materials science aims to produce function-optimized materials. Bio-inspired structures are becoming increasingly common as scientists seek to understand and replicate natural growth processes *in vitro*. Nonetheless, there remain many aspects of biomineralization that remain to be fully understood.

As examples, we present two types of biominerals that have been examined with DFXM [65]. The first relates to the nacreous layer in a mussel shell. This grows in a brick-and-mortar-like assembly, composed of calcium carbonate platelets surrounded by proteinaceous organic matrix. A piece of shell from the edge was broken off and mounted on the sample support. Examination with the dark-field microscope permitted visualization of a multitude of platelets with a large range in orientation (figure 8) [65]. Reflections were observed across the full scan range of 0.6° on both θ and in the azimuth. This unique view of the platelets *in-situ* illustrates their highly controlled assembly and inter-platelet relationships.

The second biomineral examined was fish otolith [65]. Otoliths are calcium carbonate accretions that grow in the inner ear of vertebrate fish. They are composed of aragonite fibres which extend from the nucleus to the outer surface [66]. A hierarchical structure is present, comprising the fibre, bundles of prismatic crystalline units, and nanogranules. DFXM reveals evidence of all of these levels of organization (figure 9). The visible otolith fibre is $\approx 100 \mu\text{m}$ long and individual bundles of prismatic crystalline units are visible along its length. The interruptions between bundles along the growth axis likely correspond to daily growth layers governed by the individuals circadian rhythm. Single crystalline units can be seen stacked side by side across the fibre. Individual nanogranules cannot be resolved, but small clusters can be seen. The prismatic crystalline units are closely oriented with respect to the growth axis, with the crystal c axes coherent to within $\pm 2^\circ$. The orientation of the a and b axes, however, appears to be isotropic, with prisms occupying a wide range of orientations around the c axis.

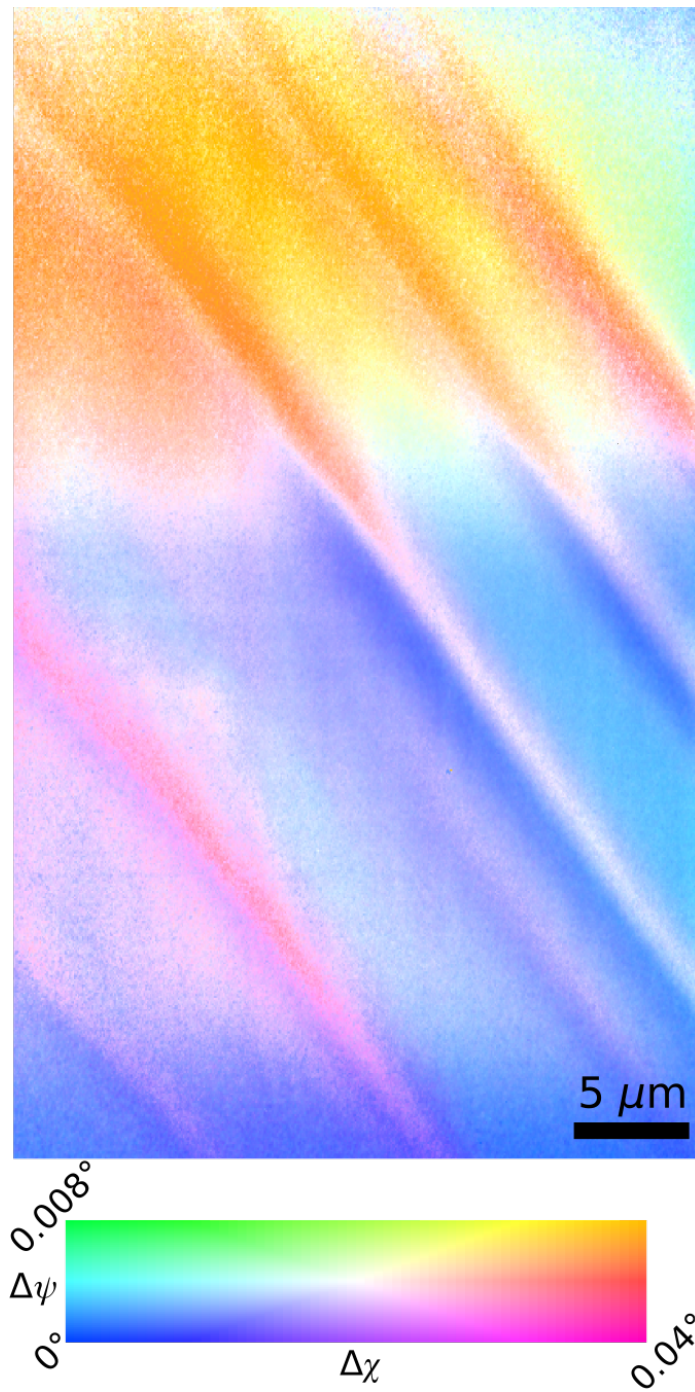


Figure 7. Dark-field x-ray microscopy images using the MLL as objective. Projection image of lattice misorientations around ferroelastic/ferroelectric domains in a BaTiO₃ single crystal. The misorientation is represented by colour according to the part of a pole figure below

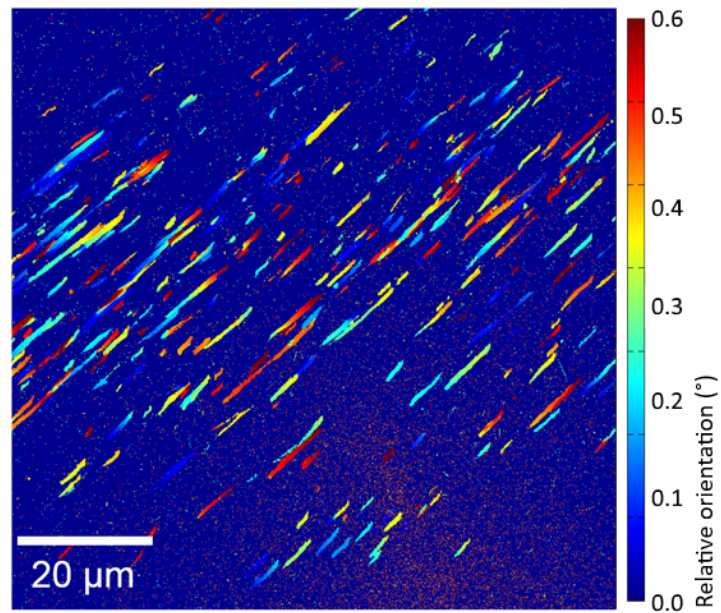


Figure 8. Orientations of nacre platelets in a mussel shell imaged by dark-field X-ray microscopy. The colours indicate orientation differences according to the scale to the right. Figure adapted from [65].

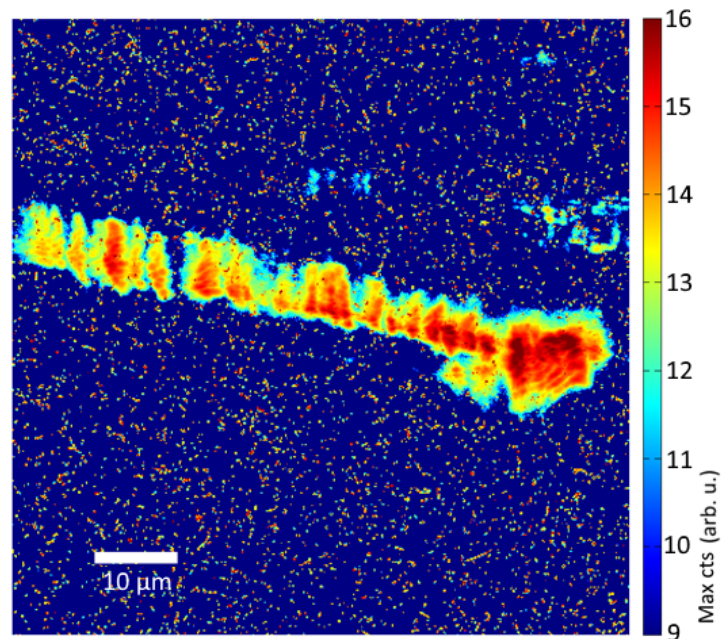


Figure 9. A dark-field image of an aragonite fibre from a fish otolith shows its growth from left to right in sequential layers, each composed of multiple crystalline units. The colour scale indicates intensity. Figure taken from [65].

Table 4. Present and future source parameters of ID06 [71]

		Present source	EBS Upgrade
Horizontal rms source size	[μm]	387.8	27.2
Horizontal rms source divergence	[μrad]	10.3	5.2
Vertical rms source size	[μm]	3.5	3.4
Vertical rms source divergence	[μrad]	1.2	1.4

4. Outlook

4.1. A multi-scale view of microstructure

Dark-field x-ray microscopy is a promising technique for multi-scale characterization of hierarchical microstructures in materials. Yet, the field of view and spatial resolution of DFXM cover only a portion of this range. Moreover, the field of view in reciprocal space is very restricted, such that only one Bragg reflection of one grain can be studied at any given time. In order to obtain a complete multi-scale view, DFXM has to be combined with complementary diffraction and imaging techniques that can provide the missing information. In particular, DCT or 3DXRD can be used to obtain three-dimensional maps of the position and orientation of all grains within a sample, with relatively lower real space and reciprocal space resolution. Acquisition of such maps would enable users to differentiate and select the relevant regions of interest (ROI) in the microstructure. Furthermore, we have ongoing work to develop a high-resolution variant of 3DXRD to bridge the gap between conventional far-field 3DXRD and DFXM.

The spatial resolution of DFXM is ultimately limited by the numerical aperture of the objective lens. In the need of higher resolution, coherent x-ray techniques such as (Bragg) coherent diffraction imaging [11, 15, 16, 13, 17, 18, 67] or Fourier ptychography [68, 69, 70] can be employed to extend DFXM towards higher spatial and reciprocal space resolution.

Common to all these techniques is that they employ hard x-rays. Therefore, it is possible, with some technical development, to perform all of the aforementioned techniques on the same instrument without the need to re-mount the sample.

The instrument at ID06 is designed with this need in mind. Efforts for on-line data analysis and integration of DCT and 3DXRD results into the DFXM data acquisition strategies are ongoing. The integration of all of the mentioned techniques is the main focus of the upcoming EBS upgrade beamline.

4.2. EBS upgrade beamline

The HXRM project has been selected for implementation as an Upgrade beamline for the ESRF EBS (Extremely Bright Source) upgrade. The microscope will be installed at a dedicated beamline with optics and infrastructure fully optimized for x-ray microscopy. We expect that the project will be implemented in 2022, and that the new beamline will be open to external users via the ESRF general user proposal system in 2023.

With the EBS upgrade [71], the source parameters will be improved significantly, as shown in table 4. In combination with a new, fully optimized undulator this will lead to a 10–30 fold increase in the maximum photon flux at the sample, but more importantly to a 200–600 fold increase in coherent flux.

The dedicated beamline will also allow pink beam operation. For bright field imaging the chromatic aberration associated with both refractive and diffractive optics can be overcome by focusing the incoming beam on the back focal plane [41], and pink beam operation can therefore lead to an increase in useful flux by two orders of magnitude. For dark field operation

a bandwidth of 1 % is not optimal, but numerical simulations indicate that it may be of relevance [72].

Acknowledgments

The authors thank Élise Dufour (UMR 7209 CNRS/Muséum National d'Histoire Naturelle) for providing otolith samples for study. We acknowledge the Karlsruhe Nano Micro Facility (KNMF) at Karlsruhe Institute of Technology (KIT) for the provision of SU-8 polymer lenses and DTU Nanolab for provision of a Si based condenser. We acknowledge the S. Bajt at the CFEL for the provision of the multilayer Laue lenses. The authors thank Tao Zhou for assistance during Fe-N experiment and the loan of SU-8 polymer lenses.

References

- [1] Liu H H, Schmidt S, Poulsen H F, Godfrey A, Liu Z Q, Sharon J A and Huang X 2011 *Science* **332** 833–834
- [2] Midgley P A and Dunin-Borkowski R E 2009 *Nature Materials* **8** 271–280
- [3] Zaaferani N, Raabe D, Singh R, Roters F and Zaeferrer S 2006 *Acta Mater.* **54** 1863–1876
- [4] Uchic M D, Groeber M A, Dimiduk D M and Simmons J 2006 *Scripta Mater.* **55** 23–28
- [5] Larson B C, Yang W, Ice G E, Budai J D and Tischler J Z 2002 *Nature* **415** 887–890
- [6] Hofmann F, Abbey B, Liu W, Xu R, Usher B F, Balaur E and Liu Y 2013 *Nat. Commun.* **4** 2774
- [7] Schroer C G, Kurapova O, Patommel J, Boye P, Feldkamp J, Lengeler B, Burghammer M, Riekel C, Vince L, van der Hart A and Kuchler M 2005 *Appl. Phys. Lett.* **87** 124103
- [8] Mimura H, Handa S, Kimura T, Yumoto H, Yamakawa D, Yokoyama H, Matsuyama S, Inagaki K, Yamamura K, Sano Y, Tamasaku K, Nishino Y, Yabashi M, Ishikawa T and Yamauchi K 2009 *Nat. Phys.* **6** 122–125
- [9] Ice G E, Budai J D and Pang J W L 2011 *Science* **334** 1234
- [10] Xu C, Zhang Y, Godfrey A, Wu G, Liu W, Tischler J Z, Liu Q and Juul Jensen D 2017 *Scientific Reports* **7**
- [11] Miao J, Charalambous P, Kirz J and Sayre D 1999 *Nature* **400** 342–344
- [12] Dierolf M, Menzel A, Thibault P, Schneider P, Kewish C M, Wepf R, Bunk O and Pfeiffer F 2010 *Nature* **467** 436–439
- [13] Pfeifer M A, Williams G J, Vartanyants I A, Harder R and Robinson I K 2006 *Nature* **442** 63–66
- [14] Shapiro D, Thibault P, Beetz T, Elser V, Howells M, Jacobsen C, Kirz J, Lima E, Miao H, Neiman A M and Sayre D 2005 *Proc. Nat. Acad. Sci. USA* **102** 15343–15346
- [15] Chapman H and Nugent K 2010 *Nature Phot.* **4** 833–839
- [16] Miao J, Ishikawa T, Robinson I K and Murnane M 2015 *Science* **348** 530–535
- [17] Chamard V, Stangl J, Carbone G, Diaz A, Chen G, Alfonso C, Mocuta C and Metzger T 2010 *Phys. Rev. Lett.* **104** 165501
- [18] Yau A, Cha W, Kanan M, Stephenson G and Ulvestad A 2017 *Science* **356** 739–742
- [19] Simons H, King A, Ludwig W, Detlefs C, Pantleon W, Schmidt S, Stöhr F, Snigireva I, Snigirev A and Poulsen H F 2015 *Nat. Commun.* **6** 6098
- [20] Simons H, Jakobsen A C, Ahl S R, Detlefs C and Poulsen H F 2016 *MRS Bulletin* **41** 454
- [21] Poulsen H F, Jakobsen A C, Simons H, Ahl S R, Cook P K and Detlefs C 2017 *J. Appl. Cryst.* **50** 1441
- [22] Poulsen H F, Cook P K, Leemreize H, Pedersen A F, Yildirim C, Kutsal M, Jakobsen A C, Trujillo J X, Ormstrup J and Detlefs C 2018 *J. Appl. Cryst.* **51** 1428–1436
- [23] Jakobsen A C, Simons H, Ludwig W, Yildirim C, Leemreize H, Porz L, Detlefs C and Poulsen H F 2019 *J. Appl. Cryst.* **52** 122
- [24] Mavrikakis N, Detlefs C, Cook P, Kutsal M, Campos A, Gauvin M, Calvillo P, Saikaly W, Hubert R, Poulsen H, Vaugeois A, Zapolsky H, Mangelinck D, Dumont M and Yildirim C 2019 *Acta Materialia* **174** 92–104
- [25] Poulsen H F, Nielsen S F, Lauridsen E M, Schmidt S, Suter R M, Lienert U, Margulies L, Lorentzen T and Juul Jensen D 2001 *J. Appl. Cryst.* **34** 751
- [26] Schmidt S, Nielsen S F, Gundlach C, Margulies L, Huang X and Juul Jensen D 2004 *Science* **305** 229–232
- [27] Jakobsen B 2006 *Science* **312** 889–892
- [28] Hefferan C M, Lind J, Li S F, Lienert U, Rollett A D and Suter R M 2012 *Acta Mater.* **60** 4311–4318
- [29] Pokharel R 2018 *Overview of High-Energy X-Ray Diffraction Microscopy (HEDM) for Mesoscale Material Characterization in Three-Dimensions* (OSTI, 2018)
- [30] King A, Johnson G, Engelberg D, Ludwig W and Marrow J 2008 *Science* **321** 382–385
- [31] Ludwig W, Reischig P, King A, Herbig M, Lauridsen E M, Johnson G, Marrow T J and Buffiere J Y 2009 *Rev. Sci. Instrum.* **80** 033905
- [32] Snigirev A, Kohn V G, Snigireva I I and Lengeler B 1996 *Nature* **384** 49

- [33] Marschall F, Last A, Simon M, Kluge M, Nazmov V, Vogt H, Ogurreck M, Greving I and Mohr J 2014 *Journal of Physics: Conference Series* **499** 012007
- [34] Stöhr F, Wright J, Simons H, Michael-Lindhard J, Hübner J, Jensen F, Hansen O and Poulsen H F 2015 *J. Micromech. Microeng.* **25** 125013
- [35] Ludwig W, Cloetens P, Härtwig J, Baruchel J, Hamelin B and Bastie P 2001 *J. Appl. Cryst.* **34** 602–607
- [36] Lengeler B, Schroer C, Tümmler J, Benner B, Richwin M, Snigirev A, Snigireva I and Drakopoulos M 1999 *J. Synchrotron Rad.* **6** 1153–1167
- [37] Falch K V, Casari D, Di Michiel M, Detlefs C, Snigirev A, Snigireva I, Honkimäki V and Mathiesen R H 2016 *J. Mater. Sci.* **52** 3497–3507
- [38] Falch K V, Lyubomirskij M, Casari D, Detlefs C, Snigirev A, Snigireva I, Detlefs C, Di Michiel M, Lyatun I and Mathiesen R H 2018 *Ultramicroscopy* **184** 267
- [39] Simons H, Ahl S R, Poulsen H F and Detlefs C 2017 *J. Synchrotron Rad.* **24** 392
- [40] Van Vaerenbergh P, Detlefs C, Härtwig J, Lafford T A, Masiello F, Roth T, Schmid W, Wattecamps P and Zhang L 2010 *AIP Conf. Proc.* **1234** 229
- [41] Falch K V, Detlefs C, Di Michiel M, Snigireva I, Snigirev A and Mathiesen R H 2016 *Appl. Phys. Lett.* **109** 054103
- [42] Guignard J and Crichton W A 2015 *Rev. Sci. Instrum.* **86** 085112
- [43] Chavanne J, Le Bec G and Penel C 2011 *Synchrotron Rad. News* **24** 10–13
- [44] Snigirev A, Snigireva I I, Vaughan G B M, Wright J P, Rossat M, Bytchkov A and Curfs C 2009 *J. Phys. Conf. Ser.* **186** 012073
- [45] Zozulya A V, Bondarenko S, Schavkan A, Westermeier F, Grübel G and Sprung M 2012 *Opt. Express* **20** 18967
- [46] Falch K V, Detlefs C, Paganin D, Christensen M S and Mathiesen R 2019 *Opt. Express* In press
- [47] Labiche J C, Mathon O, Pascarelli S, Newton M A, Guilera Ferre G, Curfs C, Vaughan G, Homs A and Fernandez Carreiras D 2007 *Rev. Sci. Instrum.* **78** 091301
- [48] Coan P, Peterzol A, Fiedler S, Ponchut C, Labiche J C and Bravin A 2006 *J. Synchrotron Rad.* **13** 260–270
- [49] Serebrennikov D, Clementyev E, Semenov A and Snigirev A 2016 *J. Synchrotron Rad.* **23** 1315–1322
- [50] Schroer C G and Lengeler B 2005 *Phys. Rev. Lett.* **94**(5) 054802
- [51] Simons H, Stöhr F, Michael-Lindhart J, Jensen F, Hansen O, Detlefs C and Poulsen H F 2015 *Opt. Commun.* **359** 460
- [52] Murray K T, Pedersen A F, Mohacsi I, Detlefs C, Morgan A J, Prasciolu M, Yildirim C, Simons H, Jakobsen A C, Chapman H N, Poulsen H F and Bajt S 2019 *Opt. Express* **27** 7120
- [53] Bajt S, Prasciolu M, Fleckenstein H, Domaracký M, Chapman H N, Morgan A J, Yefanov O, Messerschmidt M, Du Y, Murray K T, Mariani V, Kuhn M, Aplin S, Pande K, Villanueva-Perez P, Stachnik K, Chen J P, Andrejczuk A, Meents A, Burkhardt A, Pennicard D, Huang X, Yan H, Nazaretski E, Chu Y S and Hamm C E 2017 *Light: Science & Applications* **7** 17162–17162
- [54] Morgan A J, Prasciolu M, Andrejczuk A, Krzywinski J, Meents A, Pennicard D, Graafsma H, Barty A, Bean R J, Barthelmess M, Oberthuer D, Yefanov O, Aquila A, Chapman H N and Bajt S 2015 *Sci. Rep.* **5** 9892
- [55] Martin T and Koch A 2006 *Journal of Synchrotron Radiation* **13** 180–194
- [56] Koch A, Raven C, Spanne P and Snigirev A 1998 *J. Opt. Soc. Am. A* **15** 1940–1951
- [57] Sierra J, Poulsen H, Jørgensen P, Detlefs C, Cook P, Simons H, Jakobsen A and Bowen J 2019 *Journal of Power Sources* **413** 351–359
- [58] Ahl S, Simons H, Zhang Y, Detlefs C, Stöhr F, Jakobsen A, Juul Jensen D and Poulsen H 2017 *Scripta Materialia* **139** 87–91
- [59] Ahl S, Simons H, Detlefs C, Juul Jensen D and Poulsen H F 2019 Subgrain dynamics during recovery of partly recrystallized aluminium to be published
- [60] Yildirim C *et al.* 2019 Dark field x-ray microscopy study of in-situ annealing of a highly deformed steel sample in preparation
- [61] Tagantsev A K, Cross L E and Fousek J 2010 *Domains in ferroic crystals and thin films* vol 13 (Springer)
- [62] Catalan G, Seidel J, Ramesh R and Scott J F 2012 *Reviews of Modern Physics* **84** 119
- [63] Simons H, Haugen A B, Jakobsen A C, Schmidt S, Stöhr F, Majkut M, Detlefs C, Daniels J E, Damjanovic D and Poulsen H F 2018 *Nature Materials* **17** 814
- [64] Gilbert P U P A, Abrecht M and Frazer B H 2005 *Rev. Mineral. Geochem.* **59** 157–185
- [65] Cook P K, Simons H, Jakobsen A C, Yildirim C, Poulsen H F and Detlefs C 2018 *Microscopy and Microanalysis* **24** 8889
- [66] Dauphin Y and Dufour E 2008 *Micron* **39** 891 – 896 ISSN 0968-4328
- [67] Pedersen A F, Chamard V, Detlefs C, Zhou T, Carbone D and Poulsen H F 2018 X-ray coherent diffraction imaging with an objective lens: towards 3d mapping of thick polycrystals (*Preprint arxiv:1810.04268*)
- [68] Simons H, Poulsen H F, Guigay J P and Detlefs C 2016 X-ray fourier Ptychographic microscopy (*Preprint*)

- [arxiv:1609.037513](https://arxiv.org/abs/1609.037513))
- [69] Wakonig K, Diaz A, Bonnin A, Stampanoni M, Bergamaschi A, Ihli J, Guizar-Sicairos M and I A M 2019 *Sci. Adv.* **5** eaav0282
 - [70] Detlefs C, Beltran M A, Guigay J P and Simons H 2019 Translative lens-based full field coherent x-ray imaging (*Preprint* [arxiv:1905.01916](https://arxiv.org/abs/1905.01916))
 - [71] Dimper R, Reichert H, Raimondi P, Sanchez Ortiz L, Sette F and Susini J 2014 *The Orange book: ESRF Upgrade Programme Phase II (2015-2022)* (ESRF, Grenoble (France))
 - [72] Pedersen A F, Chamard V and Poulsen H F 2018 *Optics Express* **26** 23411